

New magnetic phase of the chiral skyrmion material Cu_2OSeO_3

F. Qian,^{1,*} L.J. Bannenberg,¹ H. Wilhelm,² G. Chaboussant,³ L. M. Debeer-Schmitt,⁴ M. P. Schmidt,⁵ A. Aqeel,^{6,†} T.T.M. Palstra,^{6,‡} E. Brück,¹ A.J.E. Lefering,¹ C. Pappas,¹ M. Mostovoy,⁶ and A. O. Leonov^{7,8}

¹*Faculty of Applied Sciences, Delft University of Technology, Mekelweg 15, 2629 JB Delft, The Netherlands*

²*Diamond Light Source Ltd., Chilton, Didcot, Oxfordshire, OX11 0DE, United Kingdom*

³*Laboratoire Léon Brillouin, CEA-Saclay, 91191 Gif sur Yvette, France*

⁴*Oak Ridge National Laboratory, Oak Ridge, Tennessee 37831, USA*

⁵*Max Planck Institute for Chemical Physics of Solids, Nöthnitzer-Straße 40, 01187 Dresden, Germany*

⁶*Zernike Institute for Advanced Materials, University of Groningen, Nijenborgh 4, 9747 AG Groningen, The Netherlands*

⁷*Chiral Research Center, Hiroshima University, Kagamiyama, Higashi Hiroshima, Hiroshima 739-8526, Japan*

⁸*Department of Chemistry, Faculty of Science, Hiroshima University, Kagamiyama, Higashi Hiroshima 739-8526, Japan*

The lack of inversion symmetry in the crystal lattice of magnetic materials gives rise to complex non-collinear spin orders through interactions of relativistic nature, resulting in interesting physical phenomena, such as emergent electromagnetism. Studies of cubic chiral magnets revealed a universal magnetic phase diagram, composed of helical spiral, conical spiral and skyrmion crystal phases. Here, we report a remarkable deviation from this universal behavior. By combining neutron diffraction with magnetization measurements we observe a new multi-domain state in Cu_2OSeO_3 . Just below the upper critical field at which the conical spiral state disappears, the spiral wave vector rotates away from the magnetic field direction. This transition gives rise to large magnetic fluctuations. We clarify the physical origin of the new state and discuss its multiferroic properties.

INTRODUCTION

Chiral magnets show a variety of periodically modulated spin states – spirals^{1,2}, triangular and square arrays of skyrmion tubes^{3–8}, and a cubic lattice of monopoles and anti-monopoles^{9,10} – which can be viewed as magnetic crystals of different symmetries and dimensionalities. These competing magnetic superstructures show high sensitivity to external perturbations, allowing for the control of phase boundaries with applied electric fields and stresses^{11,12}. The non-trivial topology of multiply-periodic magnetic states gives rise to emergent electromagnetic fields and unconventional spin, charge, and heat transport^{13–17}. The stability and small size of magnetic skyrmions as well as low spin currents required to set them into motion paved the way to new prototype memory devices^{18–22}.

Recent studies of chiral cubic materials hosting skyrmions, such as the itinerant magnets, MnSi and FeGe, and the Mott insulator, Cu_2OSeO_3 , showed that they exhibit the same set of magnetic states with one or more long-period spin modulations and undergo similar transitions under an applied magnetic field²³. This universality is a result of non-centrosymmetric cubic lattice symmetry and the hierarchy of energy scales^{2,24,25}. The transition temperature T_c is determined by the ferromagnetic (FM) exchange interaction J . The relatively weak antisymmetric Dzyaloshinskii-Moriya (DM) interaction with the strength D proportional to the spin-orbit coupling constant λ , renders the uniform FM state unstable towards a helical spiral modulation^{1,26}. It determines the magnitude of the modulation wave vector \mathbf{Q} and the value of the critical field H_{C2} , above which the spiral modulation is suppressed. In contrast to low-

symmetry systems^{27,28}, the DM interaction in cubic chiral magnets does not impose constraints on the direction of the spiral wave vector². The direction of the wave vector is controlled by the applied magnetic field and magnetic anisotropies of higher order in λ . In the helical spiral phase observed at low magnetic fields, magnetic anisotropies pin the direction of \mathbf{Q} either along one of the cubic body diagonals, as in MnSi, or along the cubic axes, as in FeGe or Cu_2OSeO_3 . The competition between the Zeeman and magnetic anisotropy energies sets the critical field H_{C1} of the transition between the helical and conical spiral states, above which \mathbf{Q} is parallel to the applied magnetic field. In the multiply-periodic skyrmion crystal state, the spiral wave vectors are perpendicular to the field direction, which is favored by the non-linear interaction between the three helical spirals.

Here, we report a remarkable deviation from this well established universal behavior. By Small Angle Neutron Scattering (SANS) and magnetic measurements we observe a new low-temperature magnetic phase of Cu_2OSeO_3 . At relatively high magnetic fields, \mathbf{Q} tilts away from the magnetic field vector, \mathbf{H} , when this is directed along the [001] crystallographic direction favored by anisotropy at zero field. This transition occurs where it is least expected – at H close to H_{C2} where the dominant Zeeman interaction favors $\mathbf{Q} \parallel \mathbf{H}$ and at low temperatures where thermal spin fluctuations that can affect the orientation of \mathbf{Q} are suppressed. The re-orientation of the spiral wave vector is accompanied by strong diffuse scattering, reminiscent of the pressure-induced partially ordered magnetic state in MnSi. The instability of the conical spiral state at high applied magnetic fields can be considered as a re-entrance into the helical state, although \mathbf{Q} in the “tilted conical spiral” state is not close to

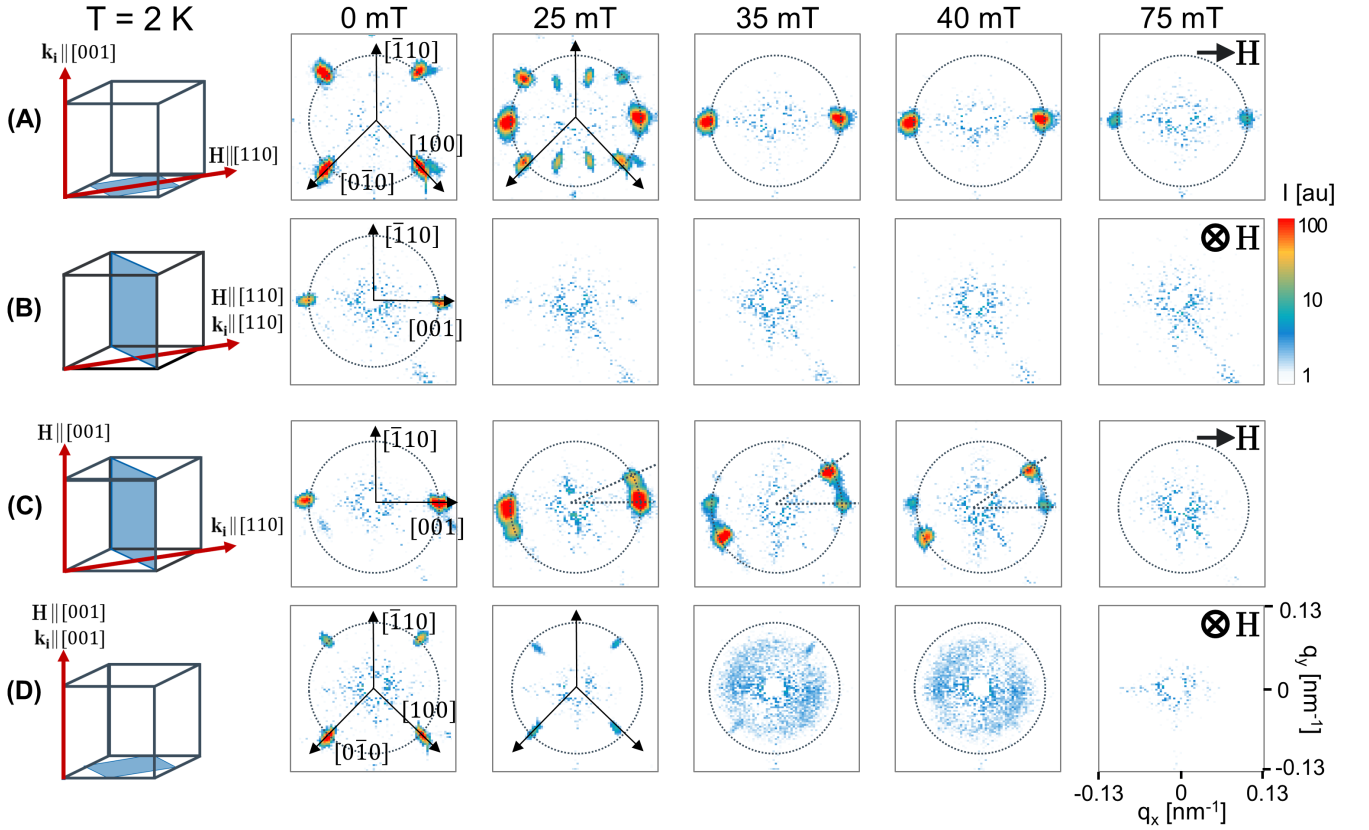


FIG. 1. **Magnetic field dependence of the Cu_2OSeO_3 SANS patterns at $T = 2$ K.** The first column illustrates the geometry of the experiment: $\mathbf{H} \parallel [110]$ in **A, B** and $\mathbf{H} \parallel [001]$ in **C, D**. The orientation of the neutron beam wavevector is: $\mathbf{k}_i \perp \mathbf{H}$ in **A, C** and $\mathbf{k}_i \parallel \mathbf{H}$ in **B, D**. The blue planes illustrate the SANS detection plane. The radius of the dashed circles on the SANS patterns corresponds to the modulus of the helical spiral propagation vector $Q = 2\pi/\ell \sim 0.1 \text{ nm}^{-1}$, with $\ell \sim 60 \text{ nm}$ being the pitch of the helix.

high-symmetry points. The new phase of Cu_2OSeO_3 is sensitive to the direction of the applied magnetic field: for $\mathbf{H} \parallel \langle 110 \rangle$ no tilted spiral state is observed. Instead, we find that the helical-to-conical spiral transition splits into two transitions occurring at slightly different magnetic fields.

We show theoretically that the tilted spiral state originates from the interplay of competing anisotropic spin interactions, which is generic to chiral magnets and may be important for understanding the structure of metastable skyrmion crystal states^{7,8,29}. This interplay is particularly strong in Cu_2OSeO_3 due to the composite nature of spin of the magnetic building blocks³⁰. The transition to the new state in multiferroic Cu_2OSeO_3 should have a strong effect on the magnetically-induced electric polarization. It should also affect the spin-Hall magnetoresistance³¹ and modify the spin-wave spectrum.

RESULTS

First hints for the existence of the new phase came from the anomalous field dependence of the magnetiza-

tion, M , and the ac magnetic susceptibilities, χ' and χ'' , shown in the Supplementary Sec. II A. A direct confirmation was provided by SANS, which probes correlations perpendicular to the incoming neutron beam wavevector \mathbf{k}_i . For this reason, we performed our measurements in two crystallographic orientations and for each orientation in two complementary configurations, $\mathbf{H} \perp \mathbf{k}_i$ and $\mathbf{H} \parallel \mathbf{k}_i$, thus providing a full picture of the effect of the magnetic field on the magnetic correlations.

A selection of patterns obtained at $T = 2$ K is shown in Fig. 1A,B for $\mathbf{H} \parallel [110]$, and Fig. 1C,D for $\mathbf{H} \parallel [001]$. At zero field the SANS patterns show four peaks along the diagonal directions in Fig. 1A,D for $\mathbf{k}_i \parallel [001]$, and two peaks along the horizontal axis in Fig. 1B,C for $\mathbf{k}_i \parallel [110]$. These are the magnetic Bragg peaks of the helical spiral state with wave vectors along the three equivalent (001) crystallographic directions.

At $\mu_0 H = 25$ mT, the scattered intensity vanishes for $\mathbf{H} \parallel \mathbf{k}_i$ (Fig. 1B,D) due to the re-orientation of the spiral wave vector along the magnetic field at the transition to the conical spiral phase. On the other hand, for $\mathbf{H} \perp \mathbf{k}_i$ and $\mathbf{H} \parallel [110]$, Fig. 1A shows the coexistence of helical spiral and conical spiral peaks (additional weak

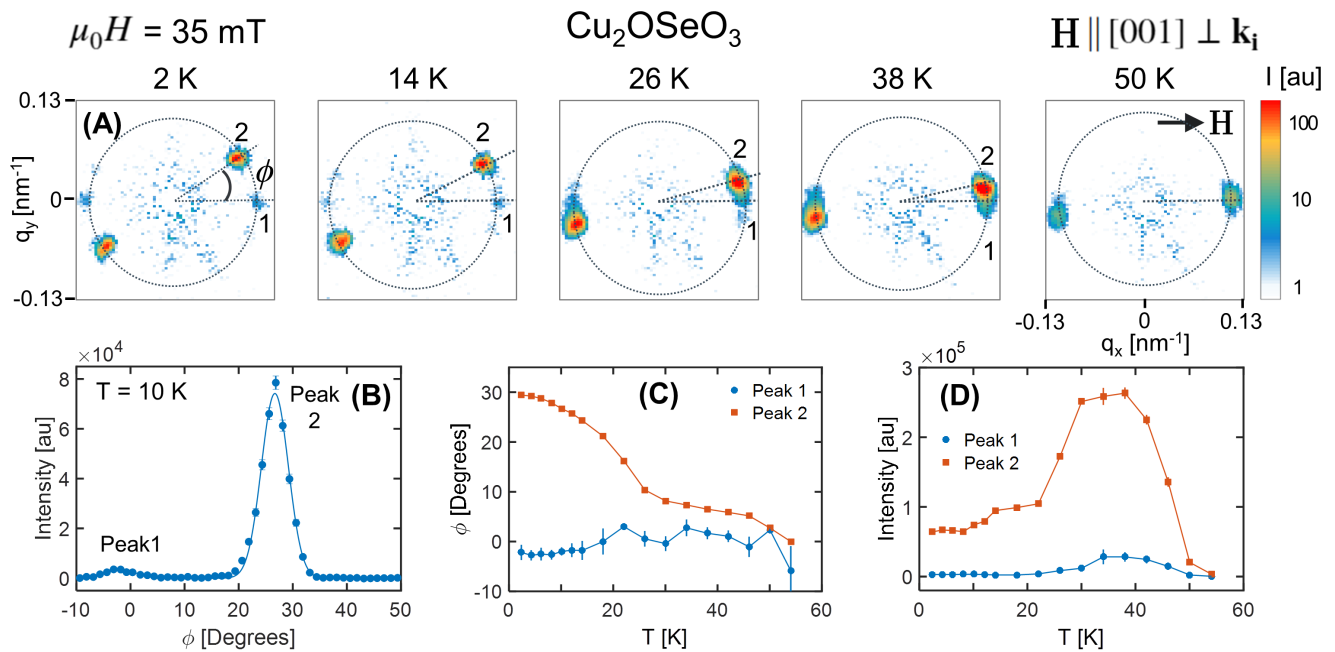


FIG. 2. **Temperature dependence of the tilt.** (A) Temperature dependence of the SANS patterns and (B-D) the corresponding data analysis. The dashed circles on the SANS patterns are a guide to the eye and have a radius of $Q = 2\pi/\ell \sim 0.1 \text{ nm}^{-1}$. The angular dependence of the scattered intensity along the circle with radius Q is given in B for $T = 10$ K. The solid lines indicate a fit with two Gaussian peaks labeled 1 and 2 in the SANS patterns. The temperature dependence of the angular positions and integrated intensities of the two peaks is shown in C and D respectively.

peaks are attributed to multiple scattering). Thus the helical-to-conical transition for $\mathbf{H} \parallel [110]$ is not a simple one-step process. Re-orientation first occurs in the helical spiral domain with the wave vector perpendicular to the field direction, $\mathbf{Q} \parallel [001]$. It is followed by a gradual re-orientation of the wave vectors of the other two helical spiral domains. Upon a further increase of the magnetic field, the conical spiral peaks weaken in intensity and disappear at the transition to the field-polarized collinear spin state, which for $\mathbf{H} \parallel \langle 110 \rangle$ occurs above 75 mT.

The unexpected behavior, signature of the new phase, is seen in the evolution of SANS patterns for $\mathbf{H} \parallel [001]$ in Fig. 1C and D. For $\mathbf{H} \perp \mathbf{k}_i$ (Fig. 1C), the Bragg peaks broaden along the circles with radius Q and eventually split into two well-defined peaks at 35 and 40 mT. This is surprising because, in this configuration the two peaks along the horizontal axis correspond to the spiral with the wave vector parallel to both the magnetic field and the cubic axis. Thus no re-orientation is expected for the spiral domain favored by both the Zeeman interaction and magnetic anisotropy. In addition to the splitting of the Bragg peaks, in the complementary configuration of $\mathbf{H} \parallel \mathbf{k}_i$ shown in Fig. 1D, a broad ring of scattering develops well inside the circle with radius Q .

With increasing temperature the splitting of the Bragg peaks becomes smaller and disappears at ~ 50 K as shown in Fig. 2A. At $T = 10$ K the scattered intensity on the circle with radius Q , when plotted against the azimuthal angle ϕ , consists of two Gaussian peaks, labeled

1 and 2 (Fig. 2B). These are centered at two distinct angles, which vary with temperature and their difference reaches 30° at $T = 2$ K (Fig. 2C). The integrated intensities depicted in Fig. 2D show that peak 2, which splits away from the conical spiral peak 1, is by far the more intense one. Its intensity goes through a maximum at ~ 35 K and then decreases at low temperatures, possibly because the optimum Bragg condition is not fulfilled any longer as the peak moves away from the magnetic field direction.

Our experimental findings are summarized in Fig. 3, which shows contour plots of the real and imaginary susceptibilities, χ' and χ'' , as well as the phase boundaries obtained by SANS. Close to T_c , the transition from the helical to the conical phase is marked by a single $\mu_0 H_{C1}(T)$ line, which at low temperatures evolves into two lines, $\mu_0 H_{C1}^{(1)}(T)$ and $\mu_0 H_{C1}^{(2)}(T)$, derived from the two adjacent χ'' peaks (see Fig. 6C,F and the discussion in the Supplement). The most prominent difference between the two field orientations appears close to $\mu_0 H_{C2}$ below 30 K. In this field and temperature range, clear maxima are seen in both χ' and χ'' for $\mathbf{H} \parallel [001]$. These define a new line $\mu_0 H_{CT}(T)$ (red dashed line in Fig. 3 D-F), which shifts slightly to lower magnetic fields with decreasing temperature.

The boundaries determined from the SANS measurements, shown in Fig. 3C,F, are in excellent agreement with those derived from susceptibility. Furthermore, it is remarkable that the shaded area in Fig. 3F, which marks

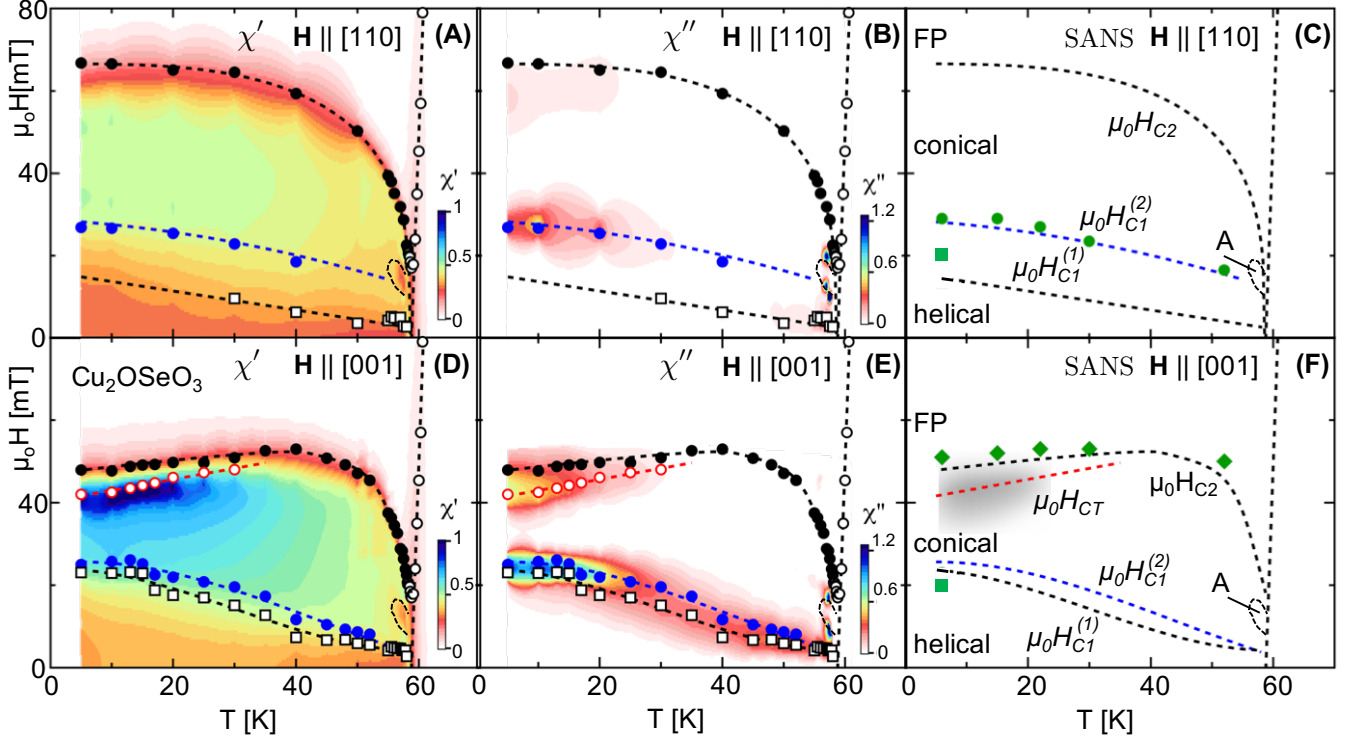


FIG. 3. **Phase diagrams from ac magnetic susceptibilities.** Contour plots of χ' and χ'' at a frequency of 10 Hz and phase boundaries obtained by SANS for $\mathbf{H} \parallel [110]$, in **A-C**, and $\mathbf{H} \parallel [001]$, in **D-F**. The units for χ' and χ'' are 10^{-4} and 10^{-6} $\text{m}^3/\text{mol}_{\text{Cu}}$, respectively. The helical, conical, A, tilted spiral (TS) and field polarized (FP) phases are indicated in **C** and **F**. The phase boundaries determined from the susceptibility are illustrated by the symbols and the dashed lines in **A, B, D, E**. They correspond to the peaks of χ'' , with the exception of $\mu_0 H_{C2}$, which is defined by the inflection point of χ' vs $\mu_0 H$. These criteria are the same as in our previous study³². At low fields, two lines $\mu_0 H_{C1}^{(1)}$ and $\mu_0 H_{C1}^{(2)}$ are identified below 50 K. Just below $\mu_0 H_{C2}$, a red dashed line denoted as $\mu_0 H_{CT}$ in **D-F**, marks the onset of the “tilted spiral” state for $\mathbf{H} \parallel \langle 001 \rangle$. The phase boundaries determined from SANS are illustrated by the green symbols in **C** and **F**. The shaded grey area just below $\mu_0 H_{C2}$ in **F** marks the region where the ring of scattering emerges for $\mathbf{H} \parallel [001] \parallel \mathbf{k}_i$.

the region, where the ring of scattering shown in Fig. 1D emerges for $\mathbf{H} \parallel \langle 001 \rangle \parallel \mathbf{k}_i$, coincides with the maxima of χ' and χ'' .

DISCUSSION

This remarkable behavior can be understood in terms of competing magnetic anisotropies that are generic to cubic chiral magnets. This competition is particularly tight in Cu_2OSeO_3 , as explained below. Despite the long history of studies of cubic chiral magnets^{2,24,25}, the discussion of anisotropic magnetic interactions in these materials remains to our best knowledge incomplete.

The starting point of our approach is a continuum model with the free energy per unit cell:

$$\mathcal{E} = \frac{Ja^2}{2} \sum_{i=x,y,z} \partial_i \mathbf{m} \cdot \partial_i \mathbf{m} + Da \mathbf{m} \cdot \nabla \times \mathbf{m} - a^3 \mu_0 M \mathbf{m} \cdot \mathbf{H} + \mathcal{E}_a, \quad (1)$$

where \mathbf{m} is the unit vector in the direction of the magnetization, M is the magnetization value, a is the lat-

tice constant, and \mathcal{E}_a is the magnetic anisotropy energy. There are five terms of fourth order in the spin-orbit coupling, λ , allowed by the $P2_13$ symmetry:

$$\begin{aligned} \mathcal{E}_a = & C_1 a^2 [\partial_x m_x \partial_x m_x + \partial_y m_y \partial_y m_y + \partial_z m_z \partial_z m_z] \\ & + C_2 a^2 [\partial_z m_x \partial_z m_x + \partial_x m_y \partial_x m_y + \partial_y m_z \partial_y m_z \\ & - (\partial_y m_x \partial_y m_x + \partial_z m_y \partial_z m_y + \partial_x m_z \partial_x m_z)] \\ & + 2C_3 a^2 [\partial_x m_x \partial_y m_y + \partial_y m_y \partial_z m_z + \partial_z m_z \partial_x m_x] \\ & + \frac{1}{2} \mathcal{J} a^4 [\partial_x^2 \mathbf{m} \cdot \partial_x^2 \mathbf{m} + \partial_y^2 \mathbf{m} \cdot \partial_y^2 \mathbf{m} + \partial_z^2 \mathbf{m} \cdot \partial_z^2 \mathbf{m}] \\ & + K (m_x^4 + m_y^4 + m_z^4). \end{aligned} \quad (2)$$

Their importance can be understood by substituting into Eq.(1) the conical spiral Ansatz:

$$\mathbf{m} = \cos \theta \mathbf{e}_3 + \sin \theta [\cos(\mathbf{Q} \cdot \mathbf{x}) \mathbf{e}_1 + \sin(\mathbf{Q} \cdot \mathbf{x}) \mathbf{e}_2], \quad (3)$$

where θ is the conical angle and $(\mathbf{e}_1, \mathbf{e}_2, \mathbf{e}_3)$ are three mutually orthogonal unit vectors. If the magnetic anisotropy and Zeeman energies are neglected, $Qa = \frac{D}{J}$ is independent of the orientation of \mathbf{Q} . The applied magnetic field favors $\mathbf{Q} \parallel \mathbf{H}$ with the conical angle given by $\cos \theta = \frac{H}{H_{C2}}$, where $\mu_0 M H_{C2} = \frac{D^2}{Ja^3}$ defines the critical field, H_{C2} .

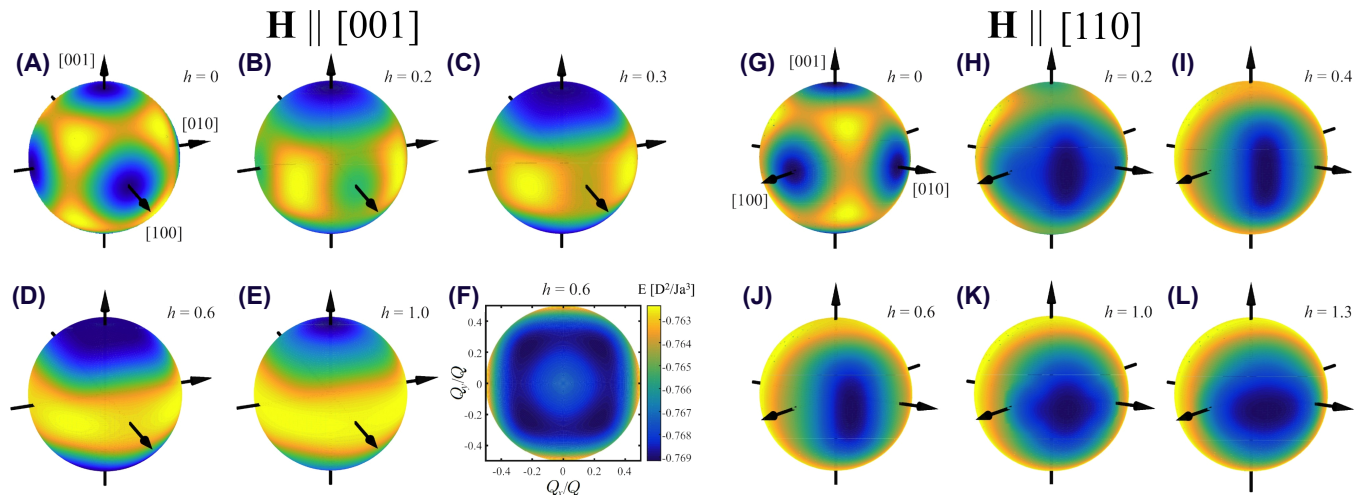


FIG. 4. **Q-dependence of spiral energy for $H||[001]$ and $H||[110]$.** False color plots of the conical spiral energy on the unit sphere of $\hat{Q} = Q/Q$ describing the direction of the spiral wave vector for various values of the dimensionless magnetic field, $h = H/H_{C2}$. (A-F) Magnetic field applied along the [001] direction: (A) $h = 0$, (B) $h = 0.2$, (C) $h = 0.3$ (D) $h = 0.6$ and (E) $h = 1.0$. (F) The energy sphere for $h = 0.6$, seen from above, showing four energy minima, which correspond to Q tilted away from the magnetic field vector along the $[\pm 1, \pm 1, 0]$ directions. (G-L) Magnetic field applied along the [110] direction: (G) $h = 0$, (H) $h = 0.2$, (I) $h = 0.4$ (J) $h = 0.6$, (K) $h = 1.0$ and (L) $h = 1.3$.

The DM interaction originates from the antisymmetric anisotropic exchange between Cu spins, which is the first-order correction to the Heisenberg exchange in powers of λ : $D \sim J\zeta$, where $\zeta = \frac{\lambda}{\Delta}$, Δ being the typical electron excitation energy on Cu sites^{26,33}. The first three anisotropy terms in Eq.(2) result from the symmetric anisotropic exchange between Cu ions and are proportional to the second power of the spin-orbit coupling^{26,33}: $C_i \sim J\zeta^2$. Since $Qa = \frac{D}{J} = \zeta$, these anisotropy terms are of order of $J\zeta^4$. The fourth term in Eq.(2) results from the expansion of the Heisenberg exchange interaction in powers of Qa and is also $\sim J\zeta^4$. The last term in Eq.(2) has the form of the fourth-order single-ion anisotropy allowed by cubic symmetry. In absence of the single-ion anisotropy for Cu ions with $S = \frac{1}{2}$, this term emerges at the scale of the unit cell containing 16 Cu ions, which form a network of tetrahedra with $S = 1$ ^{30,34}. This last term appears either as a second-order correction to the magnetic energy in powers of the symmetric anisotropic exchange or as a fourth-order correction in the antisymmetric exchange, both $\propto \zeta^4$. Importantly, the intermediate states are excited states of Cu tetrahedra³⁵ with energy $\sim J$ rather than the electronic excitations of Cu ions with energy Δ . As a result, also the last term is $\sim J\zeta^4$. Therefore, the magnetic block structure of Cu_2OSeO_3 makes all anisotropy terms in Eq.(2) comparable, which can frustrate the direction of Q .

Another important point is that the direction of Q , favored by a magnetic anisotropy term, may vary with the strength of the applied magnetic field, because it depends on the conical angle, $\theta = \theta(H)$. Supplementary Fig. 11 shows the θ -dependence of the fourth-order effective anisotropy, $K_{\text{eff}} = KB(\theta)$, which is negative for

small θ and for $\theta \sim \frac{\pi}{2}$, stabilizing the helical spiral with $Q||\langle 001 \rangle$, as it is the case for Cu_2OSeO_3 at zero field. However, for intermediate values of θ , K_{eff} is positive and the preferred direction of Q becomes $\langle 111 \rangle$. In this interval of θ , spins in the conical spiral with $Q||\langle 001 \rangle$ are closer to the body diagonals than to cubic axes, which makes this wave vector direction unfavorable (see Supplementary Sec. IID for more details).

This effect gives rise to local minima of the conical spiral energy in Q -space. If only the fourth-order anisotropy is taken into account, the global energy minimum for $H||\langle 001 \rangle$ is still at $Q||H$. However, additional anisotropy terms can turn these local minima into the global ones, so that in some magnetic field interval the tilted conical spiral becomes the ground state. Fig. 4A-F shows the false color plot of the conical spiral energy as a function of Q for several values of the dimensionless magnetic field, $h = H/H_{C2}$, applied along the [001] direction. For simplicity, only two anisotropy terms are nonzero in this calculation: $\kappa = \frac{KJ}{D^2} = -0.19$ and $\gamma_1 = \frac{C_1}{J} = -0.1$. In zero field (Fig. 4A), there are three energy minima along $\langle 001 \rangle$ i.e. along the [001], [010] and [011] directions, corresponding to three degenerate helical spiral domains in Cu_2OSeO_3 . For $h = 0.2$ (Fig. 4B), the helical spiral states with Q along the [001] and [010] directions are metastable. For $h = 0.3$ (Fig. 4C) only the minimum with $Q||[001]$ exists, corresponding to the conical spiral state. For $h = 0.6$ (Fig. 4D) the conical spiral with $Q||[001]$ is unstable and there appear four new minima, corresponding to four domains with Q tilted away from the magnetic field vector along the $[\pm 1, \pm 1, 0]$ directions, as can be seen more clearly in Fig. 4F showing the energy sphere seen from above. The relative energy changes in

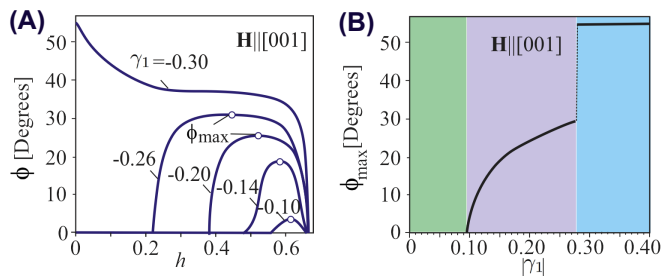


FIG. 5. **Field-induced re-orientation of the spiral wave vectors for the fourth-order anisotropy $\kappa = -0.2$ and the anisotropic exchange $\gamma_1 < 0$.** (A) Magnetic field dependence of the angle ϕ describing the tilt of the spiral wave vector \mathbf{Q} away from $\mathbf{H}||[001]$ towards the body diagonals for different values of $|\gamma_1|$. Above the critical value, $|\gamma_1| \approx 0.1$, ϕ increases from 0, that corresponds to the conical spiral phase, to a maximal value, ϕ_{max} (empty circle), and then decreases back to 0 as the magnetic field strength, h , increases. For $|\gamma_1| \gtrsim 0.28$, $\mathbf{Q}||\langle 111 \rangle$ even at zero field and smoothly rotates towards $[001]$ with increasing field. (B) Dependence of ϕ_{max} on $|\gamma_1|$. For $|\gamma_1| \lesssim 0.1$ (green area), $\phi_{max} = 0$, which implies that $\mathbf{Q}||\langle 100 \rangle$. By increasing the strength of the anisotropic exchange \mathbf{Q} smoothly rotates towards $\langle 111 \rangle$ (purple area) and for $|\gamma_1| \gtrsim 0.28$, $\mathbf{Q}||\langle 111 \rangle$ (blue area).

this part are $\sim 10^{-2}$, implying large fluctuations of the spiral wave vector, which can explain the diffuse scattering shown in Fig. 1D. Finally, Fig. 4E shows the field-polarized state at $h = 1$.

Fig. 4G-L shows the \mathbf{Q} -dependence of the conical spiral energy in several magnetic fields along the $[110]$ direction, calculated for the same values of parameters as Fig. 4A-F. As the magnetic field increases, the helical spiral states with \mathbf{Q} along the $[001]$ and $[010]$ directions merge into a single state with the wave vector parallel to \mathbf{H} and the state with $\mathbf{Q}||[001]$ ultimately disappears (see Fig. 4G,H,I). This gives rise to the two step transition from the helical to the conical phase observed experimentally. For this field direction the multi-domain tilted spiral state does not appear and there is only one global minimum with $\mathbf{Q}||\mathbf{H}||[110]$ for $H > H_{C1}$. Nevertheless, one can see the strong vertical elongation of the energy contours in Fig. 4H,I and J, which is a result of the competition with the $\mathbf{Q}||[11 \pm 1]$ states. At $h = 1$ the elongation changes from vertical to horizontal (see Fig. 4K,L).

These conclusions drawn using the variational approach are confirmed by exact energy minimization of Eq.(1) including two competing anisotropy terms: the fourth-order anisotropy with $\kappa = -0.2$ and the anisotropic exchange γ_1 . The case of $\mathbf{H}||[110]$ is treated in the Supplementary Sec. II E, which explains the two

lines, $\mu_0 H_{C1}^{(1)}$ and $\mu_0 H_{C1}^{(2)}$, for the transition from the helical to the conical spiral state, shown in Fig. 3A-C. For $\mathbf{H}||[001]$, the field dependence of the angle, ϕ , between \mathbf{Q} and the $[001]$ cubic axis, which describes the tilt of \mathbf{Q} towards the $\langle 111 \rangle$ directions is shown in Fig. 5A. The tilted spiral state appears when $|\gamma_1|$ exceeds a critical value, which is slightly lower than 0.1 for $\kappa = -0.2$. When the magnetic field increases, the tilt angle reaches its maximal value, ϕ_{max} , marked by the empty circles in Fig. 5A and then decreases to 0. As shown in Fig. 5B, $\phi_{max} = 0$ for $|\gamma_1| \lesssim 0.1$. Thus, the state with $\mathbf{Q}||\langle 100 \rangle$ is stable at low anisotropies. However, as the exchange anisotropy increases an intermediate state occurs, and finally for $|\gamma_1| \gtrsim 0.28$, the state with $\mathbf{Q}||\langle 111 \rangle$ is stabilized even at zero magnetic field.

In our diffraction experiment we do not observe all four tilted spiral domains, which is likely related to a small misalignment of the sample: due to a weak dependence of the spiral energy on \mathbf{Q} , even a tiny deviation of \mathbf{H} from the $[001]$ direction leads to the selection of one of the four domains. This suggests that the domain structure of the tilted state can also be controlled by an applied electric field using the multiferroic nature of Cu_2OSeO_3 ³⁶⁻³⁸. The electric polarization induced by the tilted spiral with the spin rotation axis $\mathbf{l} = (\frac{1}{\sqrt{2}} \sin \alpha, \frac{1}{\sqrt{2}} \sin \alpha, \cos \alpha)$ is given by:

$$\langle \mathbf{P} \rangle = \lambda \frac{(3 \cos^2 \theta - 1)}{4\sqrt{2}} \left(\sin 2\alpha, \sin 2\alpha, \frac{1}{\sqrt{2}}(1 - \cos 2\alpha) \right). \quad (4)$$

For small anisotropies, α is close to the tilt angle of \mathbf{Q} , ϕ (more precise relation between α and ϕ and the derivation of Eq.(4) can be found in Supplementary Sec. II F). Since ϕ does not exceed 30° , the induced electric polarization is almost normal to the applied magnetic field $\mathbf{H}||[001]$. The conical spiral with $\alpha = 0$ induces no electric polarization.

To summarize, we observe a new high-field multi-domain magnetic state which intervenes between the conical spiral and field-polarized phases and is stable in a broad temperature range. Its modulation vector can have four directions tilted away from the magnetic field vector applied along the high-symmetry $[001]$ direction. We show that this state is a result of the interplay between different magnetic anisotropies, generic to cubic chiral magnets. Competing anisotropies can have more general implications, such as the orientation of skyrmion tubes and the transition from the triangular to square skyrmion lattice^{7,8}. They can also play a role in the emergence of the partial order in MnSi under pressure³⁹. The transition into the tilted conical spiral phase should have many observable consequences, such as the spin-Hall magnetoresistance³¹, modified spin-wave spectrum and a magnetically-induced electric polarization.

* Nanjing University of Aeronautics and Astronautics, China

† Present Address: University of Regensburg, Germany

- [‡] Present Address: University of Twente, The Netherlands
- ¹ I. E. Dzyaloshinskii, “Theory of Helicoidal Structures in Antiferromagnets. 1. Nonmetals,” *Soviet Physics JETP* **19**, 960–971 (1964).
 - ² P. Bak and M. H. Jensen, “Theory of Helical Magnetic Structures and Phase Transitions in MnSi and FeGe,” *Journal of Physics C: Solid State Physics* **13**, L881–L885 (1980).
 - ³ A. Bogdanov and A. Hubert, “The Stability of Vortex-Like Structures in Uniaxial Ferromagnets,” *Journal of Magnetism and Magnetic Materials* **195**, 182–192 (1999).
 - ⁴ S. Mühlbauer, B. Binz, F. Jonietz, C. Pfleiderer, A. Rosch, A. Neubauer, R. Georgii, and P. Böni, “Skyrmion Lattice in a Chiral Magnet,” *Science* **323**, 915–919 (2009).
 - ⁵ X. Z. Yu, Y. Onose, N. Kanazawa, J. H. Park, J. H. Han, Y. Matsui, N. Nagaosa, and Y. Tokura, “Real-space observation of a two-dimensional skyrmion crystal,” *Nature* **465**, 901–904 (2010).
 - ⁶ A. K. Nayak, V. Kumar, T. Ma, P. Werner, E. Pippel, R. Sahoo, F. Damay, U. K. Röbber, C. Felser, and S. S. P. Parkin, “Magnetic Antiskyrmions Above Room Temperature in Tetragonal Heusler Materials,” *Nature* **548**, 561–566 (2017).
 - ⁷ K. Karube, J. S. White, N. Reynolds, J. L. Gavilano, H. Oike, A. Kikkawa, F. Kagawa, Y. Tokunaga, H. M. Rønnow, Y. Tokura, and Y. Taguchi, “Robust Metastable Skyrmions and their Triangular–Square Lattice Structural Transition in a High-Temperature Chiral Magnet,” *Nat. Mater.* **15**, 1237–1242 (2016).
 - ⁸ T. Nakajima, H. Oike, A. Kikkawa, E. P. Gilbert, N. Booth, K. Kakurai, Y. Taguchi, Y. Tokura, F. Kagawa, and T. Arima, “Skyrmion Lattice Structural Transition in MnSi,” *Science Advances* **3**, e1602562 (2017).
 - ⁹ N. Kanazawa, J.-H. Kim, D. S. Inosov, J. S. White, N. Egetenmeyer, J. L. Gavilano, S. Ishiwata, Y. Onose, T. Arima, B. Keimer, *et al.*, “Possible Skyrmion-Lattice Ground State in the B-20 Chiral-Lattice Magnet MnGe as seen via Small-Angle Neutron Scattering,” *Phys. Rev. B* **86**, 134425 (2012).
 - ¹⁰ N. Kanazawa, Y. Nii, X.-X. Zhang, A.S. Mishchenko, G. De Filippis, F. Kagawa, Y. Iwasa, N. Nagaosa, and Y. Tokura, “Critical phenomena of emergent magnetic monopoles in a chiral magnet,” *Nat. Commun.* **7**, 11622 (2016).
 - ¹¹ Y. Okamura, F. Kagawa, S. Seki, and Y. Tokura, “Transition to and from the skyrmion lattice phase by electric fields in a magnetoelectric compound,” *Nat. Commun.* **7**, 12669 (2016).
 - ¹² Y. Nii, T. Nakajima, A. Kikkawa, Y. Yamasaki, K. Ohishi, J. Suzuki, Y. Taguchi, T. Arima, Y. Tokura, and Y. Iwasa, “Uniaxial stress control of skyrmion phase,” *Nat. Commun.* **6**, 8539 (2015).
 - ¹³ M. Lee, W. Kang, Y. Onose, Y. Tokura, and N. P. Ong, “Unusual Hall Effect Anomaly in MnSi under Pressure,” *Phys. Rev. Lett* **102**, 186601 (2009).
 - ¹⁴ A. Neubauer, C. Pfleiderer, B. Binz, A. Rosch, R. Ritz, P. G. Niklowitz, and P. Böni, “Topological Hall effect in the A phase of MnSi,” *Phys Rev Lett* **102**, 186602 (2009).
 - ¹⁵ J. Zang, M. Mostovoy, J. H. Han, and N. Nagaosa, “Dynamics of Skyrmion Crystals in Metallic Thin Films,” *Phys. Rev. Lett* **107**, 136804 (2011).
 - ¹⁶ T. Schulz, R. Ritz, A. Bauer, M. Halder, M. Wagner, C. Franz, C. Pfleiderer, K. Everschor, M. Garst, and A. Rosch, “Emergent Electrodynamics of Skyrmions in a Chiral Magnet,” *Nat. Phys.* **8**, 301–304 (2012).
 - ¹⁷ N. Nagaosa and Y. Tokura, “Topological Properties and Dynamics of Magnetic Skyrmions,” *Nat. Nanotechnol.* **8**, 899–911 (2013).
 - ¹⁸ A. Fert, V. Cros, and J. Sampaio, “Skyrmions on the Track,” *Nat. Nanotechnol.* **8**, 152–156 (2013).
 - ¹⁹ W. Jiang, P. Upadhyaya, W. Zhang, G. Yu, M. B. Jungfleisch, F. Y. Fradin, J. E. Pearson, Y. Tserkovnyak, K. L. Wang, O. Heinonen, *et al.*, “Blowing magnetic skyrmion bubbles,” *Science* **349**, 283–286 (2015).
 - ²⁰ C. Moreau-Luchaire, C. Moutafis, N. Reyren, J. Sampaio, C. A. F. Vaz, N. Van Horne, K. Bouzehouane, K. Garcia, C. Deranlot, P. Warnicke, *et al.*, “Additive interfacial chiral interaction in multilayers for stabilization of small individual skyrmions at room temperature,” *Nat. Nanotechnol.* **11**, 444–448 (2016).
 - ²¹ S. Woo, K. Litzius, B. Krüger, M.-Y. Im, L. Caretta, K. Richter, M. Mann, A. Krone, R. Reeve, M. Weigand, *et al.*, “Observation of room-temperature magnetic skyrmions and their current-driven dynamics in ultrathin metallic ferromagnets,” *Nat. Mater.* **15**, 501–506 (2016).
 - ²² A. Fert, N. Reyren, and V. Cros, “Magnetic skyrmions: Advances in Physics and Potential Applications,” *Nat. Mater.* **2**, 17031 (2017).
 - ²³ A. Bauer and C. Pfleiderer, “Generic Aspects of Skyrmion Lattices in Chiral Magnets,” in *Topological Structures in Ferromagnetic Materials* (Springer International Publishing, Cham, 2016) pp. 1–28.
 - ²⁴ O. Nakanishi, A. Yanase, A. Hasegawa, and M. Kataoka, “The Origin of the Helical Spin Density Wave in MnSi,” *Solid State Communications* **35**, 995–998 (1980).
 - ²⁵ D. Belitz, T. R. Kirkpatrick, and A. Rosch, “Theory of Helimagnons in Itinerant Quantum Systems,” *Phys. Rev. B* **73**, 54431 (2006).
 - ²⁶ T. Moriya, “Anisotropic Superexchange Interaction and Weak Ferromagnetism,” *Phys. Rev.* **120**, 91–98 (1960).
 - ²⁷ Y. Togawa, T. Koyama, K. Takayanagi, S. Mori, Y. Kousaka, J. Akimitsu, S. Nishihara, K. Inoue, A. S. Ovchinnikov, and J. Kishine, “Chiral Magnetic Soliton Lattice on a Chiral Helimagnet,” *Phys. Rev. Lett* **108**, 107202 (2012).
 - ²⁸ I. Kézsmárki, S. Bordács, P. Milde, E. Neuber, L. M. Eng, J. S. White, H. M. Rønnow, C. D. Dewhurst, M. Mochizuki, K. Yanai, H. Nakamura, D. Ehlers, V. Tsurkan, and A. Loidl, “Néel-type Skyrmion Lattice with Confined Orientation in the Polar Magnetic Semiconductor GaV₄S₈,” *Nat. Mater.* **14**, 1116–1122 (2015).
 - ²⁹ L. J. Bannenberg, K. Kakurai, F. Qian, E. Lelièvre-Berna, C. D. Dewhurst, Y. Onose, Y. Endoh, Y. Tokura, and C. Pappas, “Extended skyrmion lattice scattering and long-time memory in the chiral magnet Fe_{1-x}Co_xSi,” *Phys. Rev. B* **94**, 104406 (2016).
 - ³⁰ O. Janson, I. Rousochatzakis, A. A. Tsirlin, M. Belesi, A. O. Leonov, U. K. Roessler, J. van den Brink, and H. Rosner, “The Quantum Nature of Skyrmions and Half-Skyrmions in Cu₂OSeO₃,” *Nat. Commun.* **5**, 5376 (2014).
 - ³¹ A. Aqeel, N. Vlietstra, A. Roy, M. Mostovoy, B. J. van Wees, and T. T. M. Palstra, “Electrical detection of spiral spin structures in Pt|Cu₂OSeO₃ heterostructures,” *Phys. Rev. B* **94**, 134418 (2016).
 - ³² F. Qian, H. Wilhelm, A. Aqeel, T. T. M. Palstra, A. J. E. Lefering, E. H. Brück, and C. Pappas, “Phase Diagram and Magnetic Relaxation Phenomena in Cu₂OSeO₃,” *Phys. Rev. B* **94**, 064418 (2016).

- ³³ D. Coffey, T. M. Rice, and F. C. Zhang, “Erratum: Dzyaloshinskii-Moriya interaction in the Cuprates [Phys. Rev. B **44**, 10 112 (1991)],” Phys. Rev. B **46**, 5884 (1992).
- ³⁴ J.-W. Bos, C. V. Colin, and Thomas T. M. Palstra, “Magnetoelectric Coupling in the Cubic Ferrimagnet Cu_2OSeO_3 ,” Phys. Rev. B **78**, 094416 (2008).
- ³⁵ J. Romhányi, J. van den Brink, and I. Rousochatzakis, “Entangled Tetrahedron Ground State and Excitations of the Magnetoelectric Skyrminion Material Cu_2OSeO_3 ,” Phys. Rev. B **90**, 140404(R) (2014).
- ³⁶ S Seki, S. Ishiwata, and Y. Tokura, “Magnetoelectric Nature of Skyrmions in a Chiral Magnetic Insulator Cu_2OSeO_3 ,” Phys. Rev. B **86**, 060403(R) (2012).
- ³⁷ M. Mochizuki and S. Seki, “Dynamical magnetoelectric phenomena of multiferroic skyrmions,” J. Phys.: Condens. Matter **27**, 503001 (2015).
- ³⁸ E. Ruff, P. Lunkenheimer, A. Loidl, H. Berger, and S. Krohns, “Magnetoelectric Effects in the Skyrminion Host Material Cu_2OSeO_3 ,” Sci. Rep. **5**, 15025 (2015).
- ³⁹ C. Pfleiderer, D. Reznik, L. Pintschovius, H. v. Löhneysen, M. Garst, and A. Rosch, “Partial order in the non-Fermi-liquid phase of MnSi ,” Nature **427**, 227–231 (2004).
- ⁴⁰ I Živković, D Pajić, T Ivek, and H Berger, “Two-step transition in a magnetoelectric ferrimagnet Cu_2OSeO_3 ,” Phys. Rev. B **85**, 224402 (2012).

ACKNOWLEDGMENTS

The authors acknowledge fruitful discussions with Alex Bogdanov. Dr. G. Blake and Dr. Y. Prots are acknowledged for orienting the single crystals. FQ acknowledges financial support from the China Scholarship Council. CP and LJB acknowledge NWO Groot Grant No. LARMOR 721.012.102. CP and MM acknowledge Vrije FOM-programma “Skyrmionics”. AOL thanks Ulrike Nitzsche for technical assistance and acknowledges JSPS Core-to-Core Program, Advanced Research Networks (Japan) and JSPS Grant-in-Aid for Research Activity Start-up 17H06889.

SUPPLEMENTARY MATERIALS

I. MATERIALS AND METHODS

Magnetization and magnetic susceptibility measurements were performed on two single crystals of Cu_2OSeO_3 with dimensions of $\sim 1 \times 1 \times 1 \text{ mm}^3$ grown at the Zernike Institute for Advanced Materials. One crystal was oriented with a $\langle 001 \rangle$ axis vertical while the other one was oriented with a $\langle 110 \rangle$ axis vertical. A third single crystal with dimensions $\sim 3 \times 3 \times 4 \text{ mm}^3$ grown at the Max Planck Institute for Chemical Physics of Solids was used for the neutron scattering measurements. This sample was oriented with the $[\bar{1}10]$ crystallographic axis vertical. All crystals were prepared by chemical vapor transport method and their quality and structure was checked by x-ray diffraction.

Magnetization and magnetic susceptibility were measured with a MPMS-5XL SQUID using the extraction method. For the determination of the magnetization a static magnetic field, $\mu_0 H$, was applied along the vertical direction. The real and imaginary parts of the magnetic ac susceptibility, χ' and χ'' , were measured by adding to $\mu_0 H$ a vertical drive ac field, $\mu_0 H_{ac}$, with an amplitude of 0.4 mT. The frequency of H_{ac} was varied between 0.1 and 1000 Hz.

The SANS measurements were performed on the instruments PA20 of the Laboratoire Léon Brillouin and GP-SANS of Oak Ridge National Laboratory using neutron wavelengths of 0.6 nm and 1 nm respectively. At both instruments the magnetic field was applied either parallel or perpendicular to the incoming neutron beam wave vector \mathbf{k}_i using a horizontal magnetic field cryomagnet. The orientation of the crystal axes with respect to \mathbf{k}_i and to the magnetic field was varied by rotating the sample in the cryomagnet. The SANS patterns were collected for $\mathbf{H} \parallel [110]$ and $\mathbf{H} \parallel [001]$ and, in each case, for $\mathbf{H} \perp \mathbf{k}_i$ and $\mathbf{H} \parallel \mathbf{k}_i$, by rotating both the sample and the magnetic field through 90° with respect to \mathbf{k}_i . Measurements at 70 K, where the magnetic scattering is negligible, were used for the background correction of the SANS patterns.

All measurements have been performed after zero field cooling the sample through the magnetic transition temperature, T_c , down to the temperature of interest. The magnetic field was then increased stepwise. The applied magnetic field, $\mu_0 H_{ext}$, was corrected for the demagnetizing effect to obtain the internal magnetic field, $\mu_0 H_{int}$ (in SI units):

$$\mathbf{H}_{int} = \mathbf{H}_{ext} - N\mathbf{M}, \quad (5)$$

where $N = 1/3$ is the demagnetization factor for our (nearly) cubic shape samples. The demagnetizing field correction also modifies the values of the magnetic susceptibility:

$$\chi_{int} = \frac{\chi_{ext}}{1 - \mu_0 N \chi_{ext}} \quad (6)$$

II. SUPPLEMENTARY TEXT

A. Temperature and Magnetic Field Dependence of the Magnetization and Susceptibility

Fig. 6 shows the low temperature magnetic field and temperature dependence of the magnetization M , its derivative, $\Delta M / \Delta(\mu_0 H)$, and the real and imaginary parts of the ac magnetic susceptibility, χ' and χ'' . Whereas for $\mathbf{H} \parallel [110]$ M increases almost linearly with magnetic field until saturation, clear deviations from this linear increase occur for $\mathbf{H} \parallel [001]$. These are highlighted by the emergence of peaks in the derivative, $\Delta M / \Delta(\mu_0 H)$, χ' and χ'' , which are most prominent at low temperatures and indicate complex rearrangements of spins discussed below. At low magnetic fields,

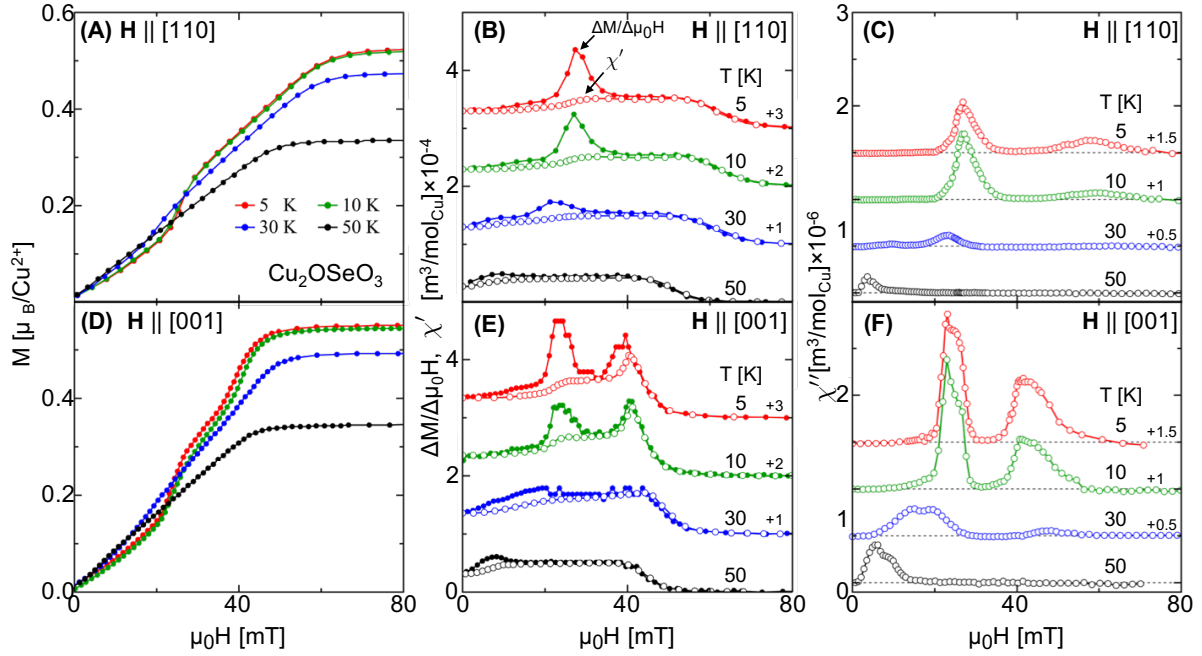


FIG. 6. **Magnetic properties of Cu_2OSeO_3 .** Magnetic field and temperature dependence of the magnetization M , its derivative, $\Delta M/\Delta(\mu_0 H)$, and the real and imaginary parts of the ac magnetic susceptibility, χ' and χ'' , at a frequency of 10 Hz for $\mathbf{H}||[110]$ (A-C) and $\mathbf{H}||[001]$ (D-F). The $\Delta M/\Delta(\mu_0 H)$, χ' and χ'' curves are shifted vertically with respect to the base line by the values indicated.

where the transition between the helical and conical spiral states is expected, $\Delta M/\Delta(\mu_0 H)$ shows a maximum, which is not seen in χ' . This discrepancy as well as the corresponding strong χ'' signal indicate strong frequency dependence and energy dissipation. A closer inspection of the frequency dependence presented below reveals that this χ'' signal is composed of two adjacent peaks, each with its own frequency dependence. At higher magnetic fields, just below the saturation of magnetization, additional peaks appear in $\Delta M/\Delta(\mu_0 H)$, χ' and χ'' but only

for $\mathbf{H}||[001]$ and $T < 30$ K. These peaks are centered at ~ 45 mT and ~ 40 mT at 30 K and 5 K, respectively, and are associated with the new unexpected state in the phase diagram of Cu_2OSeO_3 revealed by SANS.

Fig. 7 displays the temperature dependence of the magnetization for some specific magnetic fields with $\mathbf{H}||[001]$ in A and $\mathbf{H}||[110]$ in B. Besides the ZFC data from the

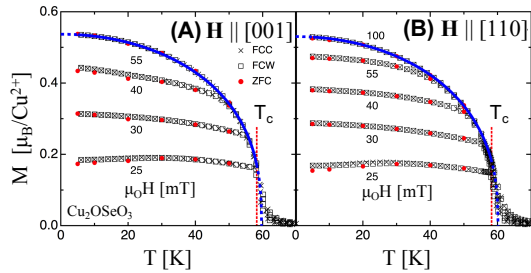


FIG. 7. **Temperature dependence of the magnetization.** The zero field cooled (ZFC) and field cooled magnetization was measured by either cooling (FCC) or warming (FCW) the sample, for $\mathbf{H}||[001]$ (A) and $\mathbf{H}||[110]$ (B). The blue lines in both panels are fits of eq. 7 with the parameters given in the Table I. The red vertical dashed lines indicate $T_c = 58.2$ K

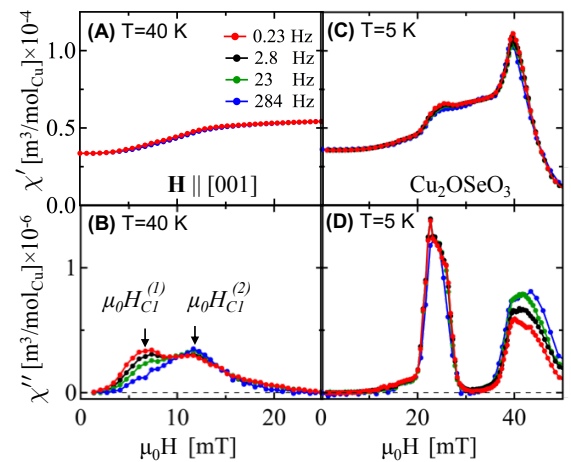


FIG. 8. χ' and χ'' as a function of magnetic field. The results are given for various frequencies at $T = 40$ K in panels (A) and (B), and $T = 5$ K in panels (C) and (D). The magnetic field was applied along $[001]$.

M vs $\mu_0 H$ curves the figure also includes magnetization points obtained by cooling the sample under magnetic field through T_c , thus following a “field cooled”, FC, protocol. These magnetization points have been measured by either cooling (FCC) or warming the sample (FCW) and do not show any noticeable dependence on the magnetic field history. The data follow a generic envelop, which is accounted for by the modified power law⁴⁰:

$$M_{sat}(T) = M_{sat}(0) [1 - (T/T_c^o)^n]^\beta, \quad (7)$$

with $M_{sat}(0)$ the saturated magnetic moment at $T = 0$ K, n and β critical exponents, and T_c^o the associated critical temperature. The fit leads to the continuous lines in Fig. 7. The fitting parameters are tabulated in Table I and are almost identical for the two sample orientations and in agreement with a previous study⁴⁰. Close to T_c , Eq. 7 reduces to the simple power law with $n = 1$), that is predicted theoretically³⁰ and mimics a 3D-Heisenberg behavior. Deviations from these generic curves occur at the $\mu_0 H_{C2}(T)$ line.

B. Frequency dependence of the ac susceptibility

The frequency dependence of the ac susceptibility is most visible for $\mathbf{H} \parallel [001]$ and in the following we will focus on the results obtained in this orientation. Fig. 8 displays χ' and χ'' measured at the indicated frequencies at 40 and 5 K. For both temperatures, χ' varies weakly with frequency and the frequency dependence is mainly visible for χ'' . At 40 K, χ'' shows two peaks which are located at 7 and 12 mT, thus close to the $\mu_0 H_{C1}(T)$ line. The amplitude of the peak at 7 mT decreases with increasing frequency, while the one at 12 mT slightly increases. At a frequency of 284 Hz only the peak at 12 mT is visible. At 5 K these two χ'' peaks seem to merge and vary very weakly with frequency. At this temperature a noticeable frequency dependence is found only for the broad peak of χ'' at ~ 40 mT, that corresponds to the tilted spiral state.

For a quantitative analysis of the frequency dependence of χ' and χ'' we considered the Cole-Cole formalism modified to include a distribution of characteristic relaxation times discussed in our previous report³²:

$$\chi(\omega) = \chi(\infty) + \frac{\chi(0) - \chi(\infty)}{1 + (i\omega\tau_0)^{1-\alpha}}, \quad (8)$$

with $\omega = 2\pi f$ the angular frequency, $\chi(0)$ and $\chi(\infty)$ the adiabatic and isothermal susceptibilities respectively and $\tau_0 = 1/(2\pi f_0)$ the characteristic relaxation time with f_0 the characteristic frequency. The parameter α measures the distribution of characteristic relaxation times with $\alpha = 0$ for a single relaxation time, and $\alpha > 0$ for a distribution of relaxation times, which becomes broader as α approaches 1. Eq. 8 leads to the in-phase and out-of-phase components of the susceptibility discussed in our previous report³².

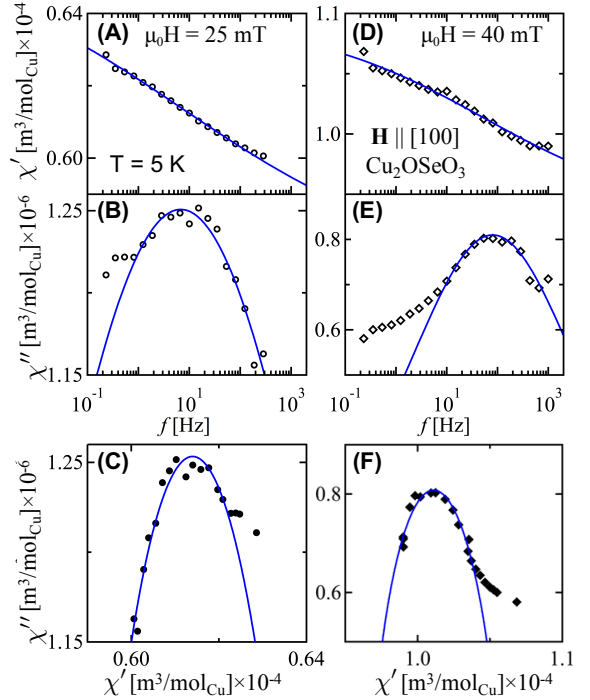


FIG. 9. **Frequency dependence of χ' and χ'' at $T = 5$ K.** The data have been collected at 25 mT (**A**, **B**) and 40 mT (**D**, **E**) and for $\mathbf{H} \parallel [001]$. The respective Cole-Cole plots of χ'' versus χ' are given in **C**, **F** where the solid lines represent fits to the Cole-Cole formalism.

Fig. 9 depicts the frequency dependence of ZFC χ' and χ'' at 5 K and for $\mu_0 H = 25$ and 40 mT. For both magnetic fields, χ' varies only slightly with frequency and decreases by no more than $\sim 3\%$ over almost four orders of magnitude in frequency. The most significant variation is found for χ'' , for which broad maxima develop around 10 Hz and 100 Hz for 25 and 40 mT respectively.

The solid lines in Fig. 9 illustrate a fit of the data to the Cole-Cole formalism. It leads to high values of α , ~ 0.85 and ~ 0.65 for $B = 25$ and 40 mT respectively, which reflect the existence of broad distributions of relaxation times. Furthermore, deviations from the simple Cole-Cole behavior occur at low frequencies indicating the presence of additional relaxation processes. This is consistent with the behavior close to T_c ³².

C. Phase boundaries determined from SANS

Fig. 10 shows the magnetic field dependence of the total scattered intensity, integrated over the detector (thus over all peaks), at $T = 6$ K. The figure shows data obtained for $\mathbf{H} \perp \mathbf{k}_i$ and collected by stepwise increasing the magnetic field. Data were also collected by stepwise decreasing the magnetic field. Both data sets are very close to each other and thus no substantial hysteresis has been found,

TABLE I. **Temperature variation of M_{sat} .** Parameters derived from the fit of Eq. 7 to the temperature dependence of M_{sat} below $T_C = 58.2$ K.

	$M_{sat}(0)$	$T_c^o - T_c$	β	n
$\mathbf{H} \parallel [001]$	0.54 (1)	1.5 (1)	0.368 (5)	1.99 (2)
$\mathbf{H} \parallel [110]$	0.53 (1)	1.8 (3)	0.391 (2)	2.01 (1)
Ref[40]	0.559 (7)	1.8 (1)	0.393 (4)	1.95

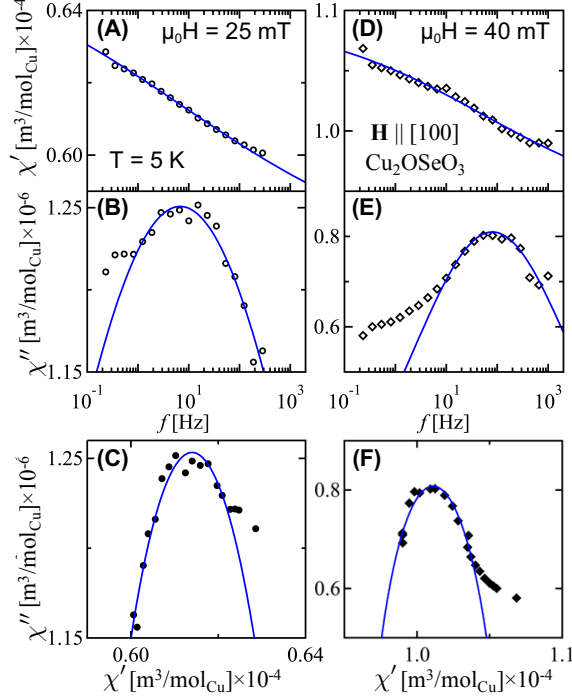


FIG. 10. **Magnetic field dependence of the SANS intensity at 6 K.** The data have been obtained by integrating over the entire detector for $\mathbf{H} \parallel [001]$ (A) and $\mathbf{H} \parallel [110]$ (B) and for $\mathbf{H} \perp \mathbf{k}_i$ (red squares) and $\mathbf{H} \parallel \mathbf{k}_i$ (black circles). The solid and open red squares correspond to data recorded by stepwise increasing and decreasing the magnetic field respectively.

In the configuration $\mathbf{H} \parallel [001]$ and $\mathbf{H} \parallel \mathbf{k}_i$ the intensity decreases sharply with increasing magnetic field and almost vanishes around 20 mT, which defines the $\mu_0 H_{C1}^{(1)}$ transition point on the phase diagram of Fig. 3F. The increase of intensity at higher magnetic fields originates from the diffuse scattering of the tilted spiral phase, which is most pronounced around 40 mT. In the complementary configuration of $\mathbf{H} \perp \mathbf{k}_i$ the total scattered intensity starts to decrease above 30 mT, i.e. in the titled spiral phase, and disappears around 50 mT, which corresponds to the $\mu_0 H_{C2}$ transition point on the phase diagram of Fig. 3. In the configuration $\mathbf{H} \parallel [110]$ and $\mathbf{H} \parallel \mathbf{k}_i$ a similar analysis leads to the determination of the $\mu_0 H_{C1}^{(1)}$ transition line. However, the $\mu_0 H_{C2}$ point could not be determined as it lies at magnetic fields that exceed the window of these measurements.

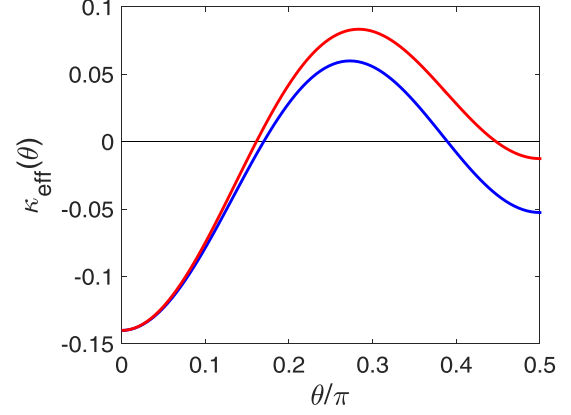


FIG. 11. **Effective anisotropy.** Effective dimensionless anisotropy for the spin rotation axis, $\kappa_{\text{eff}} = \kappa B(\theta)$, vs the conical angle, θ , for $\kappa = \frac{KJ}{D^2} = -0.14$ (blue line) and all other magnetic anisotropies equal zero. Red line shows κ_{eff} when an additional anisotropy $\gamma_1 = \frac{C_1}{J} = -0.08$ is added.

D. Effect of magnetic anisotropy on the direction of the spiral wave vector

For the conical spiral Ansatz Eq.(3), the anisotropy energy Eq.(2) equals

$$\begin{aligned} \mathcal{E}_a = & K [A(\theta) + B(\theta)(l_x^4 + l_y^4 + l_z^4)] \\ & + \frac{\sin^2(\theta)a^2}{2} \left[C_1 Q^2 - C_1 (Q_x^2 l_x^2 + Q_y^2 l_y^2 + Q_z^2 l_z^2) \right. \\ & - C_2 (Q_z^2 l_x^2 + Q_x^2 l_y^2 + Q_y^2 l_z^2) + C_2 (Q_y^2 l_x^2 + Q_z^2 l_y^2 + Q_x^2 l_z^2) \\ & \left. - 2C_3 (Q_x Q_y l_x l_y + Q_y Q_z l_y l_z + Q_z Q_x l_z l_x) \right] \\ & + \frac{\sin^2 \theta \mathcal{J} a^4}{2} (Q_x^4 + Q_y^4 + Q_z^4) \quad (9) \end{aligned}$$

with

$$\begin{cases} A(\theta) = \frac{3}{8}(1 + 6 \cos^2 \theta - 7 \cos^4 \theta), \\ B(\theta) = \frac{1}{8}(3 - 30 \cos^2 \theta + 35 \cos^4 \theta), \end{cases} \quad (10)$$

where θ is the conical spiral angle.

The blue line in Fig. 11 shows the effective dimensionless anisotropy, $\kappa_{\text{eff}}(\theta) = \frac{KJB(\theta)}{D^2}$, as a function of the conical angle for $\kappa = \frac{KJ}{D^2} = -0.14$. There is an interval of θ , in which $\kappa_{\text{eff}}(\theta) > 0$, which favors \mathbf{l} and \mathbf{Q} along a body diagonal rather than along the cubic axes.

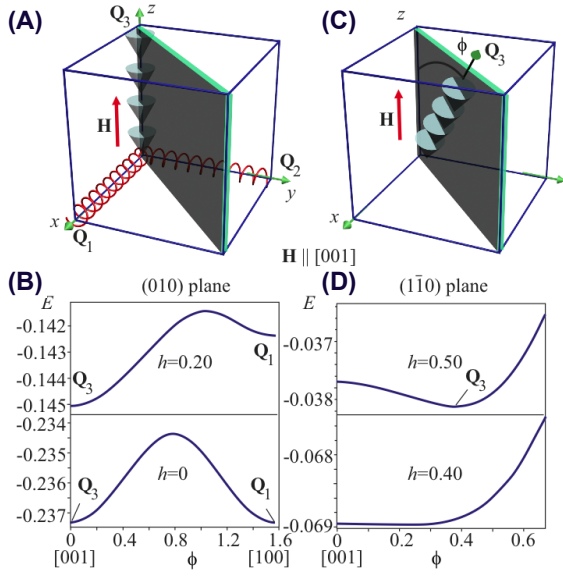


FIG. 12. **Spiral re-orientation for $H\parallel[001]$.** (A) Three spiral domains in low magnetic fields. (B) ϕ -dependence of the spiral energy density for \mathbf{Q} varying in the (010) plane in zero field and at $h = 0.2$. The global energy minimum is reached at $\mathbf{Q}_3\parallel[001]$ (ϕ is given in radians). (C) Tilted-spiral state that appears above a critical value of the magnetic field, in which \mathbf{Q} rotates away from the magnetic field vector towards the $\langle 111 \rangle$ directions. (D) Energy density plotted as a function of the tilt angle in the $(\bar{1}\bar{1}0)$ plane for $h = 0.4$ and $h = 0.5$.

When other magnetic anisotropies are added, $\kappa_{\text{eff}}(\theta)$ is defined as the coefficient in front of $\hat{Q}_x^4 + \hat{Q}_y^4 + \hat{Q}_z^4$, where $\hat{Q} = \mathbf{Q}/Q$. To leading order in the spin-orbit coupling constant, λ , $\kappa_{\text{eff}}(\theta) = \kappa B(\theta) - \frac{\gamma}{2} \sin^2 \theta$, where $\gamma = \gamma_1 - \gamma_3 + \gamma_4$ with $\gamma_i = C_i/J$ ($i = 1, 2, 3$) and $\gamma_4 = \frac{\mathcal{J}Q^2 a^2}{J}$. The red line in Fig. 11 shows $\kappa_{\text{eff}}(\theta)$, for $\kappa = -0.14$ and $\gamma = \gamma_1 = -0.08$. Negative γ widens the interval of positive $\kappa_{\text{eff}}(\theta)$ and increases the magnitude of $\kappa_{\text{eff}}(\theta) > 0$ and stabilizes the tilted spiral state in some interval of magnetic field close to H_{C2} .

E. Numerical studies of spiral re-orientation processes in presence of competing anisotropies

In this section we present more results on the spiral re-orientation processes obtained by exact energy minimization. We consider the dimensionless fourth-order and exchange anisotropies, $\kappa = \gamma_1 = -0.20$, and the magnetic field \mathbf{H} applied along the [001] and [110] directions. Figs. 12 and 13a, c schematically show a layout of \mathbf{Q} -vectors in stable and metastable spiral states with respect to the field and crystallographic directions, whereas Figs. 12 and 13b,d demonstrate the energy densities of skewed spiral states depending on the \mathbf{Q} -vector direction as calculated in particular crystallographic planes. We consider the stable orientations of \mathbf{Q} vectors in the (010)

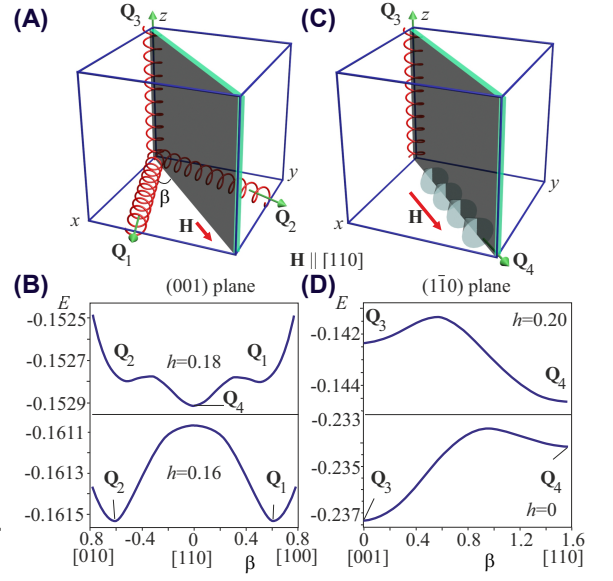


FIG. 13. **Spiral re-orientation for $H\parallel[110]$.** (A) The three helical spiral states in low magnetic fields. Under an applied magnetic field, the spiral states with \mathbf{Q}_1 and \mathbf{Q}_2 (along the [100] and [010] directions in zero field, respectively) undergo a first-order phase transition into the conical phase with $\mathbf{Q}_4\parallel\mathbf{H}$ (C), whereas the metastable spiral with the wave vector $\mathbf{Q}_3\parallel[001]$ persists up to a higher magnetic field. (B) Dependence of energy density on the angle β , given in radians, in between the spiral wave vector and the field direction below and above the first-order phase transition for \mathbf{Q} varying in the (001) plane. β -dependence of the energy density for \mathbf{Q} varying in the $(\bar{1}\bar{1}0)$ plane in zero field and at $h = 0.2$.

and $(\bar{1}\bar{1}0)$ planes, Fig. 12, and in the (001) and $(\bar{1}\bar{1}0)$ planes, Fig. 13.

$H\parallel[001]$: Fig. 12 shows the three helical spiral domains with the wave vectors $\mathbf{Q}_1, \mathbf{Q}_2$ and \mathbf{Q}_3 along the cubic axes corresponding to the global minima of the energy functional Eq. 1 in zero field. In the applied magnetic field, the spirals with $\mathbf{Q}_1\parallel[100]$ and $\mathbf{Q}_2\parallel[010]$, represented in Fig. 12A by red springs, become metastable. The stable conical spiral with $\mathbf{Q}_3\parallel[001]$ is represented by blue cones. Fig. 12B shows the dependence of spiral energy on the angle, ϕ , between \mathbf{Q} and the [001] axis, for \mathbf{Q} varying in the (010) plane. The wave vectors of the metastable spirals remain parallel to [100] and [010] these states become unstable at $h = 0.32$. Above a critical field value, the conical spiral with $\mathbf{Q} = \mathbf{Q}_3$ begins to tilt towards one of the four body diagonals, the [111] directions, as shown in Fig. 12C. Fig. 12D shows the dependence of spiral energy on the tilt angle for \mathbf{Q} varying in the $(\bar{1}\bar{1}0)$ plane, for $h = 0.4$ and $h = 0.5$. As h increases, ϕ grows, reaches its maximal value and then decreases back to zero, corresponding to a return into the conical spiral state. The maximal tilt angle, ϕ_{max} , which depends on the ratio of the competing fourth-order and exchange anisotropies, is plotted in Fig. 5 of the main text.

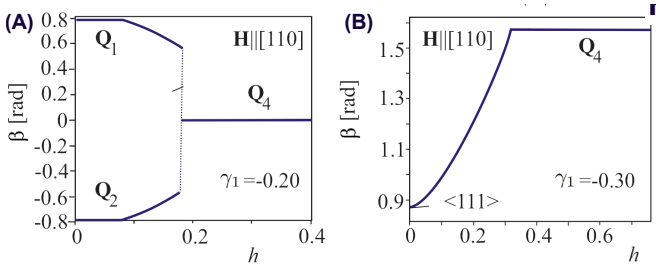


FIG. 14. **Field-induced re-orientation of the spiral wave vectors for $H\parallel[001]$ and for the fourth-order anisotropy $\kappa = -0.2$ and the anisotropic exchange $\gamma_1 < 0$.** (A) Field-dependence of the angle β between the spirals in the $[001]$ plane and $H\parallel[110]$. The smooth rotation of the spirals along Q_1 and Q_2 , which at zero field are parallel to $[100]$ and $[010]$ respectively, is followed by a discontinuous transition into the conical spiral state with $Q_4\parallel H\parallel[110]$ (a more detailed representation is given in Fig. 13). (B) Smooth rotation of the spiral vector from $\langle 111 \rangle$ towards $H\parallel[110]$ as a function of the magnetic field for a stronger exchange anisotropy, $\gamma_1 = -0.3$.

$H\parallel[110]$: The zero-field degeneracy of the helical spiral state is lifted in a different way when $H\parallel[110]$. Fig. 13A shows the three spiral domains with the wave vectors Q_1, Q_2 and Q_3 in low magnetic fields. The magnetic field favors the wave vectors Q_1 and Q_2 in the (001) -plane. Fig. 13B shows the energy density at $h = 0.16$ and $h = 0.18$ as a function of β , the angle between Q_1 and the field direction. The first-order phase transition between the helical spiral states with the wave vectors Q_1 and Q_2 and the conical spiral state with the wave vector $Q_4\parallel H$ (Fig. 13C) occurs at $h = 0.176$. The smooth field evolution of β and the subsequent jump into the state with $\beta = 0$, corresponding to the first-order phase transition, are shown in Fig. 14A of the main text. Under an applied magnetic field, the helical spiral state with $Q_3\parallel[001]$ is metastable and its wave vector is field-independent. It becomes unstable at $h = 0.34$ (Fig. 13D). The disappearance of the helical spiral states first with $Q = Q_{1,2}$ and then with $Q = Q_3$ explains the two distinct transition lines in the experimental phase diagrams (Fig. 3A-C) marked by $H_{C1}^{(1)}$ and $H_{C1}^{(2)}$.

F. Electric polarization

The electric polarization, P , induced by a magnetic ordering in Cu_2OSeO_3 is given by:³⁷

$$P = (P_a, P_b, P_c) = \lambda(m_b m_c, m_c m_a, m_a m_b), \quad (11)$$

where λ is the magneto-electric coupling and a, b and c label the three cubic axes. Using Eq.(3) and averaging over the period of the spiral, we obtain

$$\langle m_i m_j \rangle = \frac{1}{2} [\sin^2 \theta \delta_{i,j} + (3 \cos^2 \theta - 1) l_i l_j], \quad (12)$$

where $l = e_3$ is the spin rotation axis, θ is the conical angle and $i, j = a, b, c$. From Eqs. (11) and (12) one finds that the conical spiral state with $l = \hat{c} = [001]$ does not induce an electric polarization. Next we consider the tilted spiral state with $Q = (\frac{1}{\sqrt{2}} \sin \phi, \frac{1}{\sqrt{2}} \sin \phi, \cos \phi)$, where ϕ is the tilt angle (here we chose one of the four domains, in which Q tilts towards the $[111]$ axis). In the model with the fourth-order and exchange anisotropies the spin rotation axis is:

$$l = \left(\frac{1}{\sqrt{2}} \sin \alpha, \frac{1}{\sqrt{2}} \sin \alpha, \cos \alpha \right), \quad (13)$$

where α is related to ϕ by:

$$\tan \phi = \tan \alpha \frac{(1 + \gamma_1 \sin^2 \alpha)}{(1 + \gamma_1 (1 - \frac{1}{2} \sin^2 \alpha))}. \quad (14)$$

The average electric polarization induced by the tilted spiral is then given by Eq.(4).